N-type Polycrystalline Germanium Layers Formed by Impurity-Doped Solid-Phase Growth

Koki Nozawa,[†] *Takeshi Nishida,*[†] *Takamitsu Ishiyama*,[†] *Takashi Suemasu*,[†] *Kaoru Toko*[*,†]

[†] Institute of Applied Physics, University of Tsukuba, 1-1-1 Tsukuba, Ibaraki 305-8573, Japan

[*] Corresponding author: toko@bk.tsukuba.ac.jp

ABSTRACT

The carrier mobility of polycrystalline Ge thin-film transistors has significantly improved in recent years, raising hopes for the realization of next-generation electronic devices. Here, we adapted advanced solid-phase crystallization, which achieved the highest hole mobility of the polycrystalline semiconductor layer, to Ge layers doped with n-type impurities (P, As, and Sb). The type and amount of dopants had marked effects on the growth morphology and electrical properties of the Ge layers because they altered the activation energies in crystal growth, dopant activation rates, and grain boundary properties. In particular, P doping was effective in increasing the grain size (25 μm) and lowering the grain boundary barrier height (20 meV), which improved the electron density (8.0×10^{18} cm^{-3}) and electron mobility (380 cm^2 V^{-1} s^{-1}) in n-type polycrystalline Ge layers. The electron mobility is greater than that of most semiconductor layers synthesized at low temperatures (≤ 500 °C) on insulators, and this will pave the way for advanced electronic devices, such as multifunctional displays and three-dimensional large-scale integrated circuits.

KEYWORDS: *Germanium, polycrystalline thin film, solid-phase crystallization, impurity doping, high carrier mobility*

INTRODUCTION

As the scaling limits of Si complementary metal-oxide-semiconductors (CMOS) have become more severe, the implementation of channel materials with high carrier mobility is long-awaited. Because of its high carrier mobility for both electrons and holes and compatibility with conventional Si processing, Ge is the leading candidate.[1,2] In recent Ge MOS field-effect transistors, gate stack technology has enabled high field-effect mobility,[3–5] while Ge-on-insulator (GOI) technology suppressed leakage current originating from the narrow band gap.[6–8] Therefore, in terms of device performance, Ge-CMOS has the potential to sufficiently outperform conventional Si-CMOS. However, single-crystal GOI technologies, such as mechanical transfer,[9,10] oxidation-induced condensation,[6] and rapid-melting growth[11–14] require a single-crystal wafers or high temperature processes (>900 °C). To integrate Ge-CMOS into electronic devices, including three-dimensional large-scale integrated circuits or flat panel displays, it is necessary to form a high-quality Ge layer at low temperatures that does not damage the substrate or surrounding devices. Fortunately, the crystallization temperature of Ge is lower than that of Si, and many low-temperature synthesis methods have been proposed, including solid-phase crystallization (SPC),[15–17] laser annealing,[18–23] chemical vapor deposition,[24,25] lamp annealing,[26,27] plasma irradiation,[28] seed layer technique,[29] and metal-induced crystallization.[30–34] Although these methods produce polycrystalline Ge layers containing grain boundaries, large grain size and grain boundary control enable quasi-single-crystal channels in transistors.[20,21,28,32] Most of these polycrystalline Ge films are p-type, whereas reports on n-type Ge have been limited. This is because Ge tends to be p-type owing to the high density (10^{17}–10^{18} cm^{-3}) of acceptor defects[35,36] and low n-type dopant activation rates.[37,38] Therefore, the synthesis of high-quality polycrystalline Ge layers is essential for obtaining n-type Ge layers in low-temperature processes.

In recent years, the hole mobility of p-type polycrystalline Ge layers has been remarkably

improved by controlling the amorphous precursor states in SPC.[39–42] We demonstrated a p-channel thin-film transistor (TFT), which was the highest performing low-temperature TFT using a polycrystalline Ge layer.[43,44] The high crystallinity also contributed to the reduction of acceptor defects[42,45] and increased the dopant activation rate, which achieved n-type conduction control using Sb and As as dopants.[46,47] In this study, we examined the SPC of P-doped amorphous Ge layers for the first time and compared the effects of dopant species on the growth behavior and electrical properties of Ge layers. Appropriate amounts of P-doping improved the grain size and electron mobility μ_n of the Ge layer, demonstrating the best characteristics of the low-temperature n-type Ge layer.

RESULTS AND DISCUSSION

In the SPC of Ge layers, the precursor deposition temperature, T_d, is a highly influential parameter.[40] Therefore, we first investigated the effects of T_d on the SPC of the P-, As-, and Sb-doped samples. Here, the dopant concentration C_d for each impurity was fixed at approximately 3.0×10^{20} cm^{-3}. Figure 1a shows the inverse pole figure (IPF) maps of the samples crystallized at a growth temperature, T_g, of 450 °C for 5 h. The grain size significantly depended on both the dopant type and T_d, whereas the crystal orientation was almost random for all samples. Figure 1b shows the average grain size of Ge determined by the electron backscattering diffraction (EBSD) analysis. Most impurity-doped samples showed larger grain sizes than the undoped Ge. For the Sb-doped samples, the grain size peaked at 125 °C, as for undoped Ge, which was affected by the density of the precursor Ge layer.[40] In contrast, the grain sizes of the P- and As-doped samples increased with decreasing T_d. This behavior is the same as that of the Sn-doped Ge layers, which is explained by the impurity doping enhancing the density and lateral growth of amorphous Ge.[39,41] The electrical properties of the samples were evaluated by Hall measurements using the Van der Pauw method. Figure 1c shows the electron density n for

each sample. We note that only Sb-doped Ge at T_d = 50 °C showed p-type conduction, while the other samples showed n-type conduction. Considering that polycrystalline Ge layers with small grain sizes have high hole densities, this behavior can be attributed to the electrons produced by Sb doping being compensated by holes originating from the grain boundaries. For the P- and As-doped samples, which exhibited μm-order grain sizes over the entire T_d range, n was nearly constant, regardless of T_d. Figure 1d shows the activation rate of the dopants calculated from n in Figure 1c. The activation rate depended on the dopant species and was the highest for P and lowest for Sb. This behavior is consistent with that of n-type dopants in bulk single-crystal Ge (sc-Ge) and therefore attributed to the basic physical properties reflecting the solid solubility and diffusion rate of the dopants in Ge.[37,38] Figure 1e shows the μ_n for each sample. For all samples with n-type conduction, μ_n decreased with decreasing T_d. This behavior is consistent with the grain size trend shown in Figure 1b, where we consider that the carriers are affected by grain boundary scattering. However, the difference in μ_n values for different dopant species cannot be explained only by differences in grain size. In general, the higher the carrier density of a polycrystalline semiconductor film, the higher the carrier mobility, owing to the reduction of grain boundary barriers.[48–50] Considering the trend of μ_n in Figure 1c, it is reasonable that the Sb-doped sample showed a lower μ_n, and the P-doped sample had a higher μ_n, depending on the grain size. We continued the experiments with the T_d values (50 °C for As and 125 °C for P and Sb) which showed the largest μ_n for each dopant species.

Raman measurements were performed to further evaluate the dopant-dependent differences in the crystallinity of the Ge layers. Figure 2a shows the Raman spectra obtained from the P-, As-, and Sb-doped samples with C_d of approximately 3.0×10^{20} cm^{-3}. All samples showed Raman spectra containing sharp peaks attributed to crystalline Ge, but not broad peaks attributed to amorphous Ge. The crystalline Ge peaks were almost symmetrical, suggesting that the Ge layers were completely crystallized. The Raman shifts and full width at half maximum

(FWHM) of the crystalline Ge peaks were determined from the Raman spectra and are summarized in Figure 2b. All the peaks shifted to lower wavenumbers than those of the bulk single-crystal Ge substrate. There are two possible causes of the peak redshift in the polycrystalline layers: in-plane tensile strain[51–53] and phonon confinement in the nanocrystal.[54,55] Considering that the grain size of the current Ge layers is on the order of μm (Figure 1), the peak redshift is due to the tensile strain in the Ge layer. The strain value was determined to be 0.65% from the equation proposed by Manganelli *et al*.,[53] while that caused by the thermal expansion difference between the Ge and the SiO_2 substrate at the growth temperature of 450 °C was 0.34%. Therefore, the tensile strain likely reflected the transitions from amorphous to crystalline phase of Ge, in addition to the thermal expansion difference against the substrate. This behavior is consistent with our previous study on the strains in undoped Ge layers.[56] The FWHM, which indicates higher crystallinity with smaller size, was smaller for P, As, and Sb in that order. Considering the dopant activation rate shown in Figure 1d, it is possible that inactive interstitial impurities reduced the crystallinity of Ge.

We investigated the effect of C_d on the growth behavior of SPC for each dopant. Figure 3a shows that the grain size of the Ge layer after crystallization is highly dependent on both the dopant species and C_d. For all dopant species, the grain size peaked at approximately $C_d = 3.0 \times 10^{20}$ cm^{-3}. The C_d value was also roughly consistent with the Sn concentration, which maximized the Ge grain size.[41] Although it is still uncertain what determines the optimum C_d value, the phenomenon that the addition of elements to SPC precursors increases the grain size seems to be highly universal.[57] Figure 3b shows that as the grain size increases, the Ge layers are slightly oriented in the 100 and 111 planes, which have relatively low interfacial energies.[58,59] This result suggests that bulk nucleation, which provides random orientation, is suppressed, while interface nucleation becomes dominant, resulting in an enlarged Ge grain size. The Ge grain size was the largest in the P-doped sample, reaching 25 μm, which is the

largest among the Ge layers formed by SPC.

In SPC, the grain size is determined by the balance between the nucleation rate and lateral growth velocity. To explain the dependence of the Ge grain size on the dopant species and C_d, we used a neural network trained with the algorithm we had previously developed.[60] Figure 4a shows representative optical micrographs of the SPC process of the amorphous Ge layer. With an increase in the annealing time, the Ge crystals nucleated, grew laterally, and covered the entire substrate. Figures 4b and c show the annealing time dependence of nuclear density and domain size analyzed by the neural network, where the annealing temperatures were 350 °C, 375 °C, and 400 °C. As the annealing time increased, the domain size and nuclear density increased and then saturated. This behavior was strongly dependent on the annealing temperature: lower annealing temperatures resulted in lower nuclear densities and, therefore, larger domain sizes. These are the general SPC behaviors.[15,40] Figures 4d shows the Arrhenius plots of the nucleation rate and lateral growth velocity for the P-, As-, and Sb-doped samples. For each sample, the nucleation rate and lateral growth velocity were approximated by straight lines, indicating that the SPC followed an activation reaction.[61,62] The activation energies required for nucleation, $E_{nucleation}$, and lateral growth, E_{growth}, were calculated from the slopes of these lines. The results in Figures 4e and f show that $E_{nucleation}$ and E_{growth} were significantly dependent on both dopant species and C_d. The $E_{nucleation}$ of the As-doped sample showed a peak for C_d. This behavior is likely explained by the fact that metal atoms in Ge inhibit Ge lattice formation, whereas excess metal weakens the bonds in amorphous Ge.[31,63] Because the extent of such effects depends on the element type, it is possible that the peaks observed in the As-doped sample are shifted to high C_d in the P-doped sample and low C_d in the Sb-doped sample. E_{growth} was minimum around $C_d = 1.0 \times 10^{20}$ cm^{-3} for all dopant species. The phenomenon that an appropriate amount of impurity increases the growth rate is also known in the SPC of Si, which was interpreted to be due to dopant atoms.[57] The energy values in Figures 4e and f are

consistent with the grain sizes in Figure 3, considering that, in principle, the larger the $E_{nucleation}$ and the smaller the E_{growth}, the larger the grain size.[59–62]

For the samples doped with P, As, and Sb, the C_d dependence of the electrical properties was evaluated. Figure 5a shows that μ_n depended on C_d for all dopant species and peaked around $C_d = 2.0 \times 10^{20}$ cm^{-3}. This behavior is consistent with the grain size behavior shown in Figure 3, indicating that μ_n is predominantly limited by the grain boundary scattering of electrons.[48–50] Figure 5b shows the C_d dependence of n. We note that C_d of Sb lower than 9.0×10^{20} cm^{-3} provided p-type Ge layers. For the P and As samples, n increased with increasing C_d concentration and then began to decrease. Figure 5c shows that the activation rate decreased with increasing C_d concentrations. This behavior may be due to the segregation of dopants with increasing C_d, especially at the grain boundaries.[64] n, and the activation rates were the largest for P and the smallest for Sb. This behavior is consistent with the basic properties reflecting the solid solubility and diffusion rate of the dopants in Ge.[37,38] After the SPC at 450 °C, we performed post annealing (PA) at 500 °C for all samples, which was effective in reducing acceptor defects in the p-type Ge layer and increasing hole mobility.[42] Figure 5d shows that μ_n improved in most samples. In contrast, Figures 5e and f show that n and the apparent activation rate after PA decreased for P, increased for As, and remained unchanged for Sb. Considering that high-temperature PA will increase the activation rate, reduce the acceptor defects, and evaporate some dopants, these balances probably resulted in the behavior shown in Figures 5e and f.

We investigated the effect of the dopant type and C_d on the grain boundary properties of n-type Ge layers by analyzing the temperature dependence of the electrical properties using the Evans and Nelson model.[49,50] The trap-state density Q_t and energy barrier height E_B of the grain boundary can be quantified using the following equations:

$$Q_t = \frac{8\varepsilon E_B}{Lq^2} \ , \qquad (1)$$

$$\mu_n = \frac{Lq}{k_B T} \frac{v_r}{1+\frac{v_r}{v_d}} \exp\left(-\frac{E_B}{k_B T}\right) \ , \qquad (2)$$

where ε is the dielectric permittivity, L is the grain size, q is the elementary charge, v_r is the recombination velocity, v_d is the drift diffusion velocity, and k_B is Boltzmann's constant. Although v_r and v_d are temperature-dependent parameters, they are negligible when the carrier concentration is sufficiently high (> 10^{14} cm^{-3}).[50] As shown in Figure 6a, the Arrhenius plots of $\mu_n T$ are downward-sloping straight lines for all the samples. These results indicate that μ_n is limited by the grain boundary scattering of electrons. Figure 6b shows that the behavior of Q_t with respect to C_d was similar to that of the grain size in Figure 3. This behavior may be due to the facts that an appropriate amount of dopant atoms compensates for dangling bonds at grain boundaries, while excessive amounts of dopant atoms precipitate at grain boundaries and increase defects.[41] The latter effect is more likely to occur in Ge with a smaller grain size and in dopants with lower solubility limits.[64] Figure 6c shows that E_B tended to reflect Q_t and n. The Q_t and E_B values of the As- and P-doped samples were slightly reduced by PA. This behavior is interpreted as passivation of grain boundary traps, as in the p-type Ge layer.[36] In contrast, PA increased the Q_t and E_B values of the Sb-doped sample, possibly because of the segregation of Sb, which has a high diffusion coefficient at the grain boundaries.[37,38] The E_B values together with the grain size in Figure 3 account for the trend of μ_n in Figures 5a and b. The μ_n and n values are summarized in Figure 6d. A higher value of n provided a higher value of μ_n. This behavior is the same as that of general polycrystalline semiconductor thin films,[48] whereas it is the opposite of that of polycrystalline p-Ge layers.[40,42] In polycrystalline semiconductor thin films, where carrier mobility is limited by grain boundary scattering, an increase in carrier density causes a decrease in E_B, and therefore, an increase in carrier mobility. Conversely, in p-Ge layers, owing to their small E_B, hole mobility shows the opposite trend because the effect of impurity scattering is more dominant than grain boundary scattering. The current behavior of μ_n with respect to n reflects not only the decrease in E_B with increasing n

but also that it is easier to obtain a higher n with larger grain sizes. In the Ge layers doped with P, which have relatively high activation rates, μ_n was significantly higher than that of single-crystal Si and comparable to that of single-crystal Ge at the same n.

CONCLUSIONS

We investigated the doping effect of n-type impurities (P, As, and Sb) in amorphous Ge on the subsequent low-temperature SPC for the fabrication of n-type polycrystalline Ge layers. The type and amount of dopant had remarkable effects on the growth behavior and electrical properties of the Ge layer. Neural network analysis of the growth behavior showed that P addition on the order of 10^{20} cm^{-3} resulted in high $E_{nucleation}$ and low E_{growth}, resulting in large grains (25 μm). The relatively high activation rate of P allowed for a high n and low E_B approaching 10^{19} cm^{-3} and 20 meV, respectively, which resulted in high electron mobility (380 cm^2 V^{-1} s^{-1}). This electron mobility is higher than that of most semiconductor layers on insulators and single-crystal Si for $n > 10^{18}$ cm^{-3}. This achievement will enable the realization of Ge-based high-speed thin-film transistors and CMOS devices used in advanced multifunctional displays and three-dimensional large-scale integrated circuits.

METHODS

Sample preparation. In the experiments, P-, As-, and Sb-doped Ge precursors were deposited on SiO_2 glass substrates using the Knudsen cell of a molecular beam deposition system (base pressure:5×10^{-7} Pa). The Ge thickness was 200 nm and Ge deposition rate was fixed at 3.4 nm min^{-1}. The temperature of the substrate during deposition, T_d, ranged from 50 to 175 °C. T_d spontaneously increased from room temperature to 50 °C, even though the substrate was not heated; this was due to the heat radiation from the Knudsen cell. The samples were then loaded into a conventional tube furnace under an N_2 (99.9%) atmosphere and annealed at a growth

temperature, T_g, of 350–450 °C to induce crystallization. PA was performed at 500 °C for 5h, under Ar atmosphere.

Material characterization. Raman spectroscopy was performed using a JASCO NRS-5100 (laser wavelength:532 nm, spot size:5 μm), where the laser power (0.5 mW) was sufficiently weak to not affect the crystal phase and peak shift. In *situ* optical microscopy during annealing was performed using a Linkam 10042 D microscope with a Keyence VH-5500. SEM and EBSD analyses were performed using JEOL JSM-7001F (voltage:15 kV) with a TSL OIM analysis attachment. The SIMS measurements were performed using a PHI ADEPT1010 instrument. Hall effect measurement was performed by the Van der Pauw method using a Bio-Rad HL5500PC system, where μ_n and n were averaged over five measurements for each sample.

AUTHOR INFORMATION

Corresponding Author

* Electric mail: toko@bk.tsukuba.ac.jp

Notes

The authors declare no competing interests.

ACKNOWLEDGEMENTS

Part of this work was supported by NEDO (No. P14004), the TEPCO Memorial Foundation, and JSPS KAKENHI (No. 21H01358). The authors are grateful to Prof. T. Sekiguchi (University of Tsukuba) for the EBSD measurements. Some experiments were conducted at the Nanotechnology Platform.

REFERENCES

(1) Sze, S. M.; Irvin, J. C. Resistivity, Mobility and Impurity Levels in GaAs, Ge, and Si at 300°K. *Solid. State. Electron.* **1968**, *11* (6), 599–602.

(2) Prince, M. Drift Mobilities in Semiconductors. I. Germanium. *Phys. Rev.* **1953**, *92* (3), 681–687.

(3) Nayfeh, A.; Chui, C. O.; Yonehara, T.; Saraswat, K. C. Fabrication of High-Quality p-MOSFET in Ge Grown Heteroepitaxially on Si. *IEEE Electron Device Lett.* **2005**, *26* (5), 311–313.

(4) Brunco, D. P.; De Jaeger, B.; Eneman, G.; Mitard, J.; Hellings, G.; Satta, a.; Terzieva, V.; Souriau, L.; Leys, F. E.; Pourtois, G.; Houssa, M.; Winderickx, G.; Vrancken, E.; Sioncke, S.; Opsomer, K.; Nicholas, G.; Caymax, M.; Stesmans, A; Van Steenbergen, J.; Mertens, P. W.; Meuris, M.; Heyns, M. M. Germanium MOSFET Devices: Advances in Materials Understanding, Process Development, and Electrical Performance. *J. Electrochem. Soc.* **2008**, *155* (January), H552.

(5) Yamamoto, K.; Sada, T.; Wang, D.; Nakashima, H. Dramatic Enhancement of Low Electric-Field Hole Mobility in Metal Source/Drain Ge p-Channel Metal-Oxide-Semiconductor Field-Effect Transistors by Introduction of Al and Hf into SiO_2/GeO_2 Gate Stack. *Appl. Phys. Lett.* **2013**, *103* (12), 122106.

(6) Takagi, S.; Zhang, R.; Suh, J.; Kim, S.-H.; Yokoyama, M.; Nishi, K.; Takenaka, M. III–V/Ge Channel MOS Device Technologies in Nano CMOS Era. *Jpn. J. Appl. Phys.* **2015**, *54* (6S1), 06FA01.

(7) Mizubayashi, W.; Noda, S.; Ishikawa, Y.; Nishi, T.; Kikuchi, A.; Ota, H.; Su, P.-H.; Li, Y.; Samukawa, S.; Endo, K. Impacts of Plasma-Induced Damage Due to UV Light Irradiation during Etching on Ge Fin Fabrication and Device Performance of Ge Fin Field-Effect Transistors. *Appl. Phys. Express* **2017**, *10* (2), 026501.

(8) Toriumi, A.; Nishimura, T. Germanium CMOS Potential from Material and Process Perspectives: Be More Positive about Germanium. *Jpn. J. Appl. Phys.* **2018**, *57* (1), 010101.

(9) Taraschi, G.; Pitera, A. J.; Fitzgerald, E. A. Strained Si, SiGe, and Ge on-Insulator: Review of Wafer Bonding Fabrication Techniques. *Solid. State. Electron.* **2004**, *48* (8), 1297–1305.

(10) Yu, K.; Yang, F.; Cong, H.; Zhou, L.; Liu, Q.; Zhang, L.; Cheng, B.; Xue, C.; Zuo, Y.; Li, C. Fabrication of High-Hole-Mobility Germanium-on-Insulator Wafers through an Easy Method. *J. Alloys Compd.* **2018**, *750*, 182–188.

(11) Feng, J.; Thareja, G.; Kobayashi, M.; Chen, S.; Poon, A.; Bai, Y.; Griffin, P. B.; Wong, S. S.; Nishi, Y.; Plummer, J. D. High-Performance Gate-All-around GeOI p-MOSFETs Fabricated by Rapid Melt Growth Using Plasma Nitridation and ALD Al_2O_3 Gate Dielectric and Self-Aligned NiGe Contacts. *IEEE Electron Device Lett.* **2008**, *29* (7), 805–807.

(12) Hu, S.; Leu, P. W.; Marshall, A. F.; McIntyre, P. C. Single-Crystal Germanium Layers Grown on Silicon by Nanowire Seeding. *Nat. Nanotechnol.* **2009**, *4* (10), 649–653.

(13) Hosoi, T.; Suzuki, Y.; Shimura, T.; Watanabe, H. Mobility Characterization of Ge-on-Insulator Metal-Oxide-Semiconductor Field-Effect Transistors with Striped Ge Channels Fabricated by Lateral Liquid-Phase Epitaxy. *Appl. Phys. Lett.* **2014**, *105*, 173502.

(14) Toko, K.; Ohta, Y.; Tanaka, T.; Sadoh, T.; Miyao, M. Chip-Size Formation of High-Mobility Ge Strips on SiN Films by

Cooling Rate Controlled Rapid-Melting Growth. *Appl. Phys. Lett.* **2011**, *99* (3), 032103. https://doi.org/10.1063/1.3611904.

(15) Toko, K.; Nakao, I.; Sadoh, T.; Noguchi, T.; Miyao, M. Electrical Properties of Poly-Ge on Glass Substrate Grown by Two-Step Solid-Phase Crystallization. *Solid. State. Electron.* **2009**, *53* (11), 1159–1164.

(16) Tsao, C.-Y.; Huang, J.; Hao, X.; Campbell, P.; Green, M. A. Formation of Heavily Boron-Doped Hydrogenated Polycrystalline Germanium Thin Films by Co-Sputtering for Developing P+ Emitters of Bottom Cells. *Sol. Energy Mater. Sol. Cells* **2011**, *95* (3), 981–985.

(17) Jung, H.-W.; Jung, W.-S.; Yu, H.-Y.; Park, J.-H. Electrical Properties of Phosphorus-Doped Polycrystalline Germanium Formed by Solid-Phase and Metal-Induced Crystallization. *J. Alloys Compd.* **2013**, *561*, 231–233.

(18) Yeh, W.; Chen, H.; Huang, H.; Hsiao, C.; Jeng, J. Superlateral Growth of a-Ge Film by Excimer Laser Annealing. *Appl. Phys. Lett.* **2008**, *93* (9), 094103.

(19) Sakaike, K.; Higashi, S.; Murakami, H.; Miyazaki, S. Crystallization of Amorphous Ge Films Induced by Semiconductor Diode Laser Annealing. *Thin Solid Films* **2008**, *516* (11), 3595–3600.

(20) Li, Y.-S.; Liang, H.-H.; Wu, C.-Y.; Huang, W.-H.; Luo, J.-D.; Chuang, K.-C.; Li, W.-S.; Cheng, H.-C. High-Performance n-Channel Polycrystalline Germanium Thin-Film Transistors via Continuous-Wave Laser Crystallization and Green Nanosecond Laser Annealing for Source and Drain Dopant Activation. *Jpn. J. Appl. Phys.* **2019**, *58* (SD), SDDE02.

(21) Zhang, L.; Hong, H.; Yu, C.; Li, C.; Chen, S.; Huang, W.; Wang, J.; Wang, H. Poly-GeSn Junctionless Thin-Film Transistors on Insulators Fabricated at Low Temperatures via Pulsed Laser Annealing. *Phys. status solidi – Rapid Res. Lett.* **2019**, *2019*, 1900420.

(22) Takahashi, K.; Kurosawa, M.; Ikenoue, H.; Sakashita, M.; Nakatsuka, O.; Zaima, S. Dopant Behavior in Heavily Doped Polycrystalline $Ge_{1-x}Sn_x$ Layers Prepared with Pulsed Laser Annealing in Water. *Jpn. J. Appl. Phys.* **2018**, *57* (4S), 04FJ02.

(23) Matsumura, R.; Fukata, N. Self-Organized <100> Direction Growth of Germanium Film on Insulator Obtained by High Speed Continuous Wave Laser Annealing. *Mater. Lett.* **2021**, *288*, 129328.

(24) Matsui, T.; Kondo, M.; Ogata, K.; Ozawa, T.; Isomura, M. Influence of Alloy Composition on Carrier Transport and Solar Cell Properties of Hydrogenated Microcrystalline Silicon-Germanium Thin Films. *Appl. Phys. Lett.* **2006**, *89* (14), 142115.

(25) Tada, M.; Park, J.-H.; Jain, J. R.; Saraswat, K. C. Low-Temperature, Low-Pressure Chemical Vapor Deposition and Solid Phase Crystallization of Silicon–Germanium Films. *J. Electrochem. Soc.* **2009**, *156* (1), D23.

(26) Kamata, Y.; Koike, M.; Kurosawa, E.; Kurosawa, M.; Ota, H.; Nakatsuka, O.; Zaima, S.; Tezuka, T. Operation of Inverter and Ring Oscillator of Ultrathin-Body Poly-Ge CMOS. *Appl. Phys. Express* **2014**, *7* (12), 121302.

(27) Usuda, K.; Kamata, Y.; Kamimuta, Y.; Mori, T.; Koike, M.; Tezuka, T. High-Performance Poly-Ge Short-Channel Metal-Oxide-Semiconductor Field-Effect Transistors Formed on SiO_2 Layer by Flash Lamp Annealing. *Appl. Phys. Express* **2014**, *7*, 056501.

(28) Sato, T.; Hanafusa, H.; Higashi, S. Investigation on Electrical Characteristics of TFTs Fabricated with Germanium Films Crystallized by Atmospheric-Pressure Micro Thermal Plasma Jet Irradiation. *Jpn. J. Appl. Phys.* **2022**, *61* (SC), SC1011.

(29) Asadirad, M.; Gao, Y.; Dutta, P.; Shervin, S.; Sun, S.; Ravipati, S.; Kim, S. H.; Yao, Y.; Lee, K. H.; Litvinchuk, A. P.; Selvamanickam, V.; Ryou, J. H. High-Performance Flexible Thin-Film Transistors Based on Single-Crystal-Like Germanium on Glass. *Adv. Electron. Mater.* **2016**, *2* (8), 1600041.

(30) Toko, K.; Numata, R.; Oya, N.; Fukata, N.; Usami, N.; Suemasu, T. Low-Temperature (180 °C) Formation of Large-Grained Ge (111) Thin Film on Insulator Using Accelerated Metal-Induced Crystallization. *Appl. Phys. Lett.* **2014**, *104*, 022106.

(31) Wang, Z.; Jeurgens, L. P. H.; Sigle, W.; Mittemeijer, E. J. Observation and Origin of Extraordinary Atomic Mobility at Metal-Semiconductor Interfaces at Low Temperatures. *Phys. Rev. Lett.* **2015**, *115* (1), 016102.

(32) Kasahara, K.; Nagatomi, Y.; Yamamoto, K.; Higashi, H.; Nakano, M.; Yamada, S.; Wang, D.; Nakashima, H.; Hamaya, K. Electrical Properties of Pseudo-Single-Crystalline Germanium Thin-Film-Transistors Fabricated on Glass Substrates. *Appl. Phys. Lett.* **2015**, *107* (14), 142102.

(33) Suzuki, T.; Joseph, B. M.; Fukai, M.; Kamiko, M.; Kyuno, K. Low-Temperature (330 °C) Crystallization and Dopant Activation of Ge Thin Films via AgSb-Induced Layer Exchange: Operation of an n-Channel Polycrystalline Ge Thin-Film Transistor. *Appl. Phys. Express* **2017**, *10* (9), 095502.

(34) Gao, H.; Sadoh, T. Layer-Exchange Crystallization for Low-Temperature (~450 °C) Formation of n-Type Tensile-Strained Ge on Insulator. *Appl. Phys. Lett.* **2020**, *117* (17), 172102.

(35) Haesslein, H.; Sielemann, R.; Zistl, C. Vacancies and Self-Interstitials in Germanium Observed by Perturbed Angular Correlation Spectroscopy. *Phys. Rev. Lett.* **1998**, *80* (12), 2626–2629.

(36) Imajo, T.; Ishiyama, T.; Nozawa, K.; Suemasu, T.; Toko, K. Acceptor Defects in Polycrystalline Ge Layers Evaluated Using Linear Regression Analysis. *Sci. Rep.* **2022**, *12* (1), 14941.

(37) Koike, M.; Kamata, Y.; Ino, T.; Hagishima, D.; Tatsumura, K.; Koyama, M.; Nishiyama, A. Diffusion and Activation of N-Type Dopants in Germanium. *J. Appl. Phys.* **2008**, *104* (2), 023523.

(38) Sgourou, E. N.; Panayiotatos, Y.; Vovk, R. V.; Kuganathan, N.; Chroneos, A. Diffusion and Dopant Activation in Germanium: Insights from Recent Experimental and Theoretical Results. *Appl. Sci.* **2019**, *9* (12), 2454.

(39) Sadoh, T.; Kai, Y.; Matsumura, R.; Moto, K.; Miyao, M. High Carrier Mobility of Sn-Doped Polycrystalline-Ge Films on Insulators by Thickness-Dependent Low-Temperature Solid-Phase Crystallization. *Appl. Phys. Lett.* **2016**, *109* (23), 232106.

(40) Toko, K.; Yoshimine, R.; Moto, K.; Suemasu, T. High-Hole Mobility Polycrystalline Ge on an Insulator Formed by Controlling Precursor Atomic Density for Solid-Phase Crystallization. *Sci. Rep.* **2017**, *7* (1), 16981.

(41) Moto, K.; Yoshimine, R.; Suemasu, T.; Toko, K. Improving Carrier Mobility of Polycrystalline Ge by Sn Doping. *Sci. Rep.* **2018**, *8* (1), 14832.

(42) Imajo, T.; Ishiyama, T.; Saitoh, N.; Yoshizawa, N.; Suemasu, T.; Toko, K. Record-High Hole Mobility Germanium on

Flexible Plastic with Controlled Interfacial Reaction. *ACS Appl. Electron. Mater.* **2022**, *4* (1), 269–275.

(43) Moto, K.; Yamamoto, K.; Imajo, T.; Suemasu, T.; Nakashima, H.; Toko, K. Polycrystalline Thin-Film Transistors Fabricated on High-Mobility Solid-Phase-Crystallized Ge on Glass. *Appl. Phys. Lett.* **2019**, *114* (21), 212107.

(44) Moto, K.; Yamamoto, K.; Imajo, T.; Suemasu, T.; Nakashima, H.; Toko, K. Sn Concentration Effects on Polycrystalline GeSn Thin Film Transistors. *IEEE Electron Device Lett.* **2021**, *42* (12), 1735–1738.

(45) Mizoguchi, T.; Ishiyama, T.; Moto, K.; Imajo, T.; Suemasu, T.; Toko, K. Solid-Phase Crystallization of GeSn Thin Films on GeO_2 -Coated Glass. *Phys. status solidi – Rapid Res. Lett.* **2022**, *16* (1), 2100509.

(46) Takahara, D.; Moto, K.; Imajo, T.; Suemasu, T.; Toko, K. Sb-Doped Crystallization of Densified Precursor for n-Type Polycrystalline Ge on an Insulator with High Carrier Mobility. *Appl. Phys. Lett.* **2019**, *114* (8), 082105.

(47) Saito, M.; Moto, K.; Nishida, T.; Suemasu, T.; Toko, K. High-Electron-Mobility (370 cm^2/Vs) Polycrystalline Ge on an Insulator Formed by As-Doped Solid-Phase Crystallization. *Sci. Rep.* **2019**, *9* (1), 16558.

(48) Seto, J. W. Y. The Electrical Properties of Polycrystalline Silicon Films. *J. Appl. Phys.* **1975**, *46* (12), 5247–5254.

(49) Evans, P. V.; Nelson, S. F. Determination of Grain-boundary Defect-state Densities from Transport Measurements. *J. Appl. Phys.* **1991**, *69* (6), 3605–3611.

(50) Ikeda, H. Evaluation of Grain Boundary Trap States in Polycrystalline–Silicon Thin-Film Transistors by Mobility and Capacitance Measurements. *J. Appl. Phys.* **2002**, *91* (7), 4637–4645.

(51) Efremov, M. D.; Bolotov, V. V.; Volodin, V. A.; Fedina, L. I.; Lipatnikov, E. A. Excimer Laser and Rapid Thermal Annealing Stimulation of Solid-Phase Nucleation and Crystallization in Amorphous Silicon Films on Glass Substrates. *J. Phys. Condens. Matter* **1996**, *8* (3), 273–286.

(52) Efremov, M. D.; Bolotov, V. V.; Volodin, V. A.; Kochubei, S. A. Raman Scattering Anisotropy in a System of (110)-Oriented Silicon Nanocrystals Formed in a-Si Film. *Solid State Commun.* **1998**, *108* (9), 645–648.

(53) Manganelli, C. L.; Virgilio, M.; Skibitzki, O.; Salvalaglio, M.; Spirito, D.; Zaumseil, P.; Yamamoto, Y.; Montanari, M.; Klesse, W. M.; Capellini, G. Temperature Dependence of Strain–Phonon Coefficient in Epitaxial Ge/Si(001): A Comprehensive Analysis. *J. Raman Spectrosc.* **2020**, *51* (6), 989–996.

(54) Volodin, V. A.; Marin, D. V.; Sachkov, V. A.; Gorokhov, E. B.; Rinnert, H.; Vergnat, M. Applying an Improved Phonon Confinement Model to the Analysis of Raman Spectra of Germanium Nanocrystals. *J. Exp. Theor. Phys.* **2014**, *118* (1), 65–71.

(55) Volodin, V. A.; Krivyakin, G. K.; Ivlev, G. D.; Prokopyev, S. L.; Gusakova, S. V.; Popov, A. A. Crystallization of Amorphous Germanium Films and Multilayer A-Ge/a-Si Structures upon Exposure to Nanosecond Laser Radiation. *Semiconductors* **2019**, *53* (3), 400–405.

(56) Imajo, T.; Suemasu, T.; Toko, K. Strain Effects on Polycrystalline Germanium Thin Films. *Sci. Rep.* **2021**, *11* (1), 8333.

(57) Matsuyama, T.; Tanaka, M.; Tsuda, S.; Nakano, S.; Kuwano, Y. Improvement of N-Type Poly-Si Film Properties by Solid Phase Crystallization Method. *Jpn. J. Appl. Phys.* **1993**, *32* (Part 1, No. 9A), 3720–3728.

(58) Stekolnikov, A. A.; Furthmüller, J.; Bechstedt, F. Absolute Surface Energies of Group-IV Semiconductors: Dependence

on Orientation and Reconstruction. *Phys. Rev. B* **2002**, *65* (11), 115318.

(59) Toko, K.; Suemasu, T. Metal-Induced Layer Exchange of Group IV Materials. *J. Phys. D. Appl. Phys.* **2020**, *53* (37), 373002.

(60) Ishiyama, T.; Imajo, T.; Suemasu, T.; Toko, K. Machine Learning of Fake Micrographs for Automated Analysis of Crystal Growth Process. *Sci. Technol. Adv. Mater. Methods* **2022**, *2* (1), 213–221.

(61) Csepregi, L.; Küllen, R. P.; Mayer, J. W.; Sigmon, T. W. Regrowth Kinetics of Amorphous Ge Layers Created by 74Ge and 28Si Implantation of Ge Crystals. *Solid State Commun.* **1977**, *21* (11), 1019–1021.

(62) Germain, P.; Zellama, K.; Squelard, S.; Bourgoin, J. C.; Gheorghiu, A. Crystallization in Amorphous Germanium. *J. Appl. Phys.* **1979**, *50* (11), 6986–6994.

(63) Hiraki, A. LOW TEMPERATURE REACTIONS AT Si/METAL INTERFACES; WHAT IS GOING ON AT THE INTERFACES? *Surf. Sci. Rep.* **1984**, *3*, 357–412.

(64) King, A. H. Geometric and Thermodynamic Properties of Grain Boundary Junctions. *Interface Sci.* **1999**, *7* (3), 251–271.

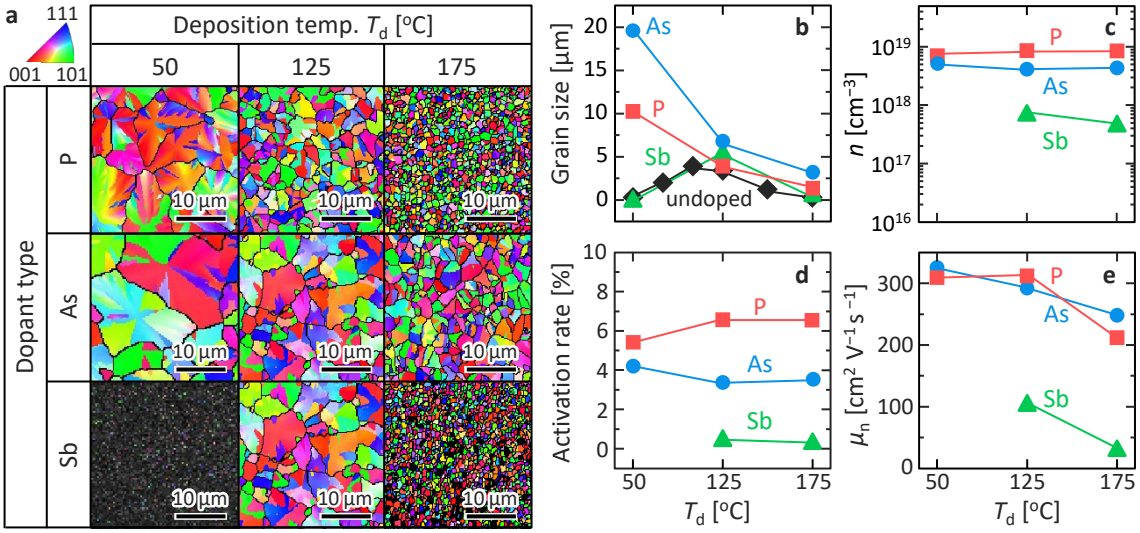

Figure 1. Grain size and electrical properties of the P-, As-, and Sb-doped Ge layers with C_d = 3.0×10^{20} cm^{-3} and T_g = 450 °C for 5 h. (a) IPF images summarized as the matrix composed of T_d (50 °C, 125 °C, and 175 °C) and dopant type (P, As, and Sb). The colors indicate the crystal orientation according to the inserted color key. T_d dependence of (b) the average grain size calculated from the EBSD analyses, (c) electron density n, (d) activation rate, and (e) electron mobility μ_n as a function of T_d. In (b), the data for undoped Ge are shown for comparison.

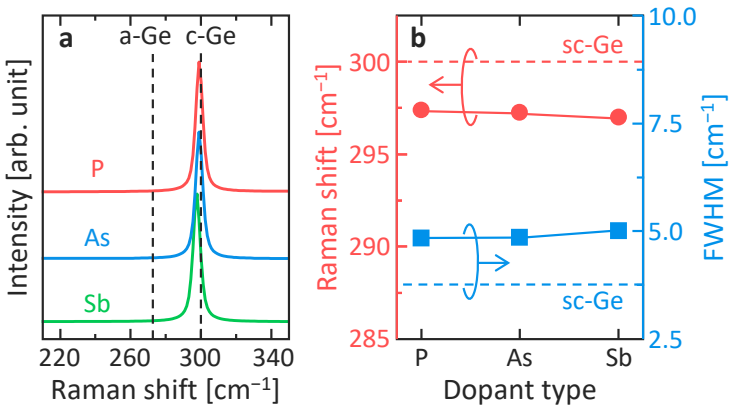

Figure 2. Raman spectroscopy study of the P-, As-, and Sb-doped samples with C_d = 3.0 × 10^{20} cm^{-3}, T_d = 50 °C (As) and 125 °C (P and Sb), and T_g = 450 °C for 5 h. (a) Raman spectra, where the dotted lines show the position of amorphous Ge (a-Ge) and crystalline Ge (c-Ge) peaks. (b) Raman shifts and FWHMs of the c-Ge peaks. The data for a bulk single-crystal Ge (sc-Ge) wafer are shown by the dotted lines.

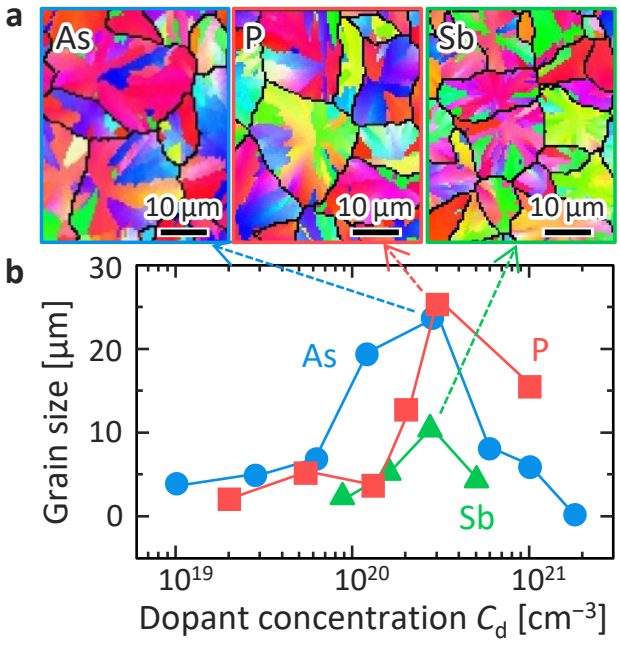

Figure 3. C_d dependence of the grain size in the P-, As-, and Sb-doped Ge layers with T_d = 50 °C (As) and 125 °C (P and Sb) and T_g = 450 °C for 5 h. (a) IPF images showing the sample with maximum grain size for each dopant. (b) Average grain size determined by the EBSD analyses as a function of C_d.

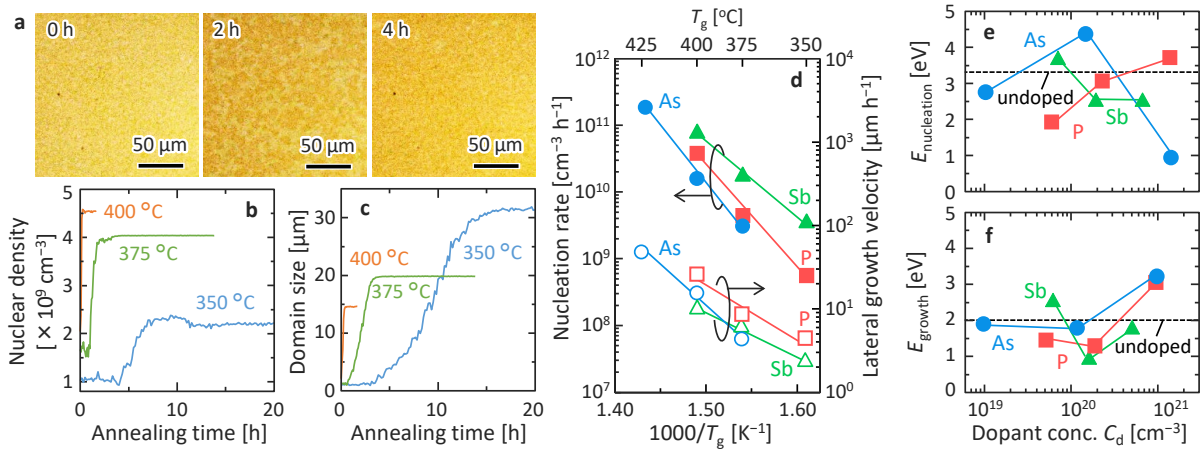

Figure 4. Characteristics of the growth properties in P-, As-, and Sb-doped Ge layers with T_d = 50 °C (As) and 125 °C (P and Sb). (a) *In situ* optical microscopy images of the P-doped sample with $C_d = 2.0 \times 10^{20}$ cm^{-3} for $T_g = 375$ °C. The light-colored area indicates amorphous Ge and the dark-colored area indicates crystalline Ge. Annealing time dependence of (b) the nuclear density and (c) the domain size analyzed by the neural network we developed.[60] (d) Arrhenius plots of the nucleation rate and lateral growth velocity. C_d dependence of the activation energies required for (e) nucleation $E_{nucleation}$ and (f) lateral growth E_{growth}. The dotted lines indicate the data of conventional undoped Ge.[61,62]

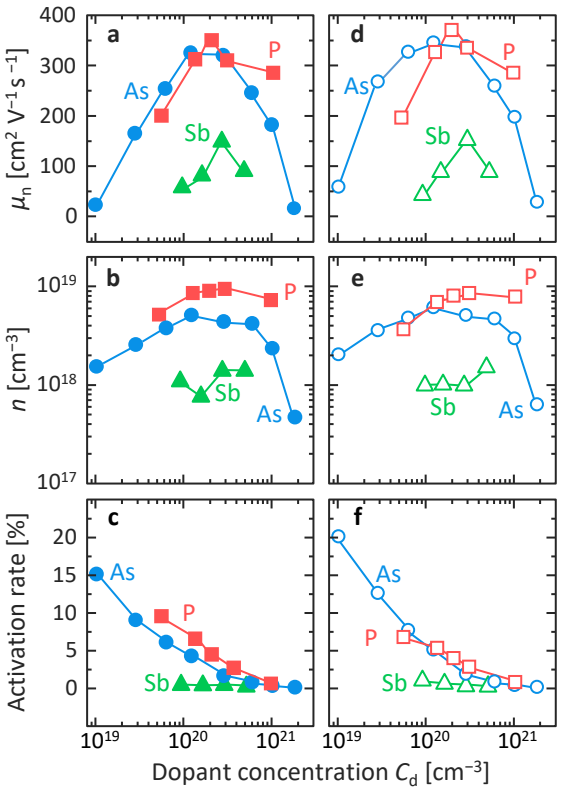

Figure 5. C_d dependence of the electrical properties of the P-, As-, and Sb-doped Ge layers with T_d = 50 °C (As) and 125 °C (P and Sb) and T_g = 450 °C for 5 h, obtained from Hall effect measurements with the Van der Pauw method. (a) Electron mobility μ_n, (b) electron concentration n, and (c) activation rate for the samples before PA. (d) μ_n, (e) n, and (f) activation rate for the samples after PA.

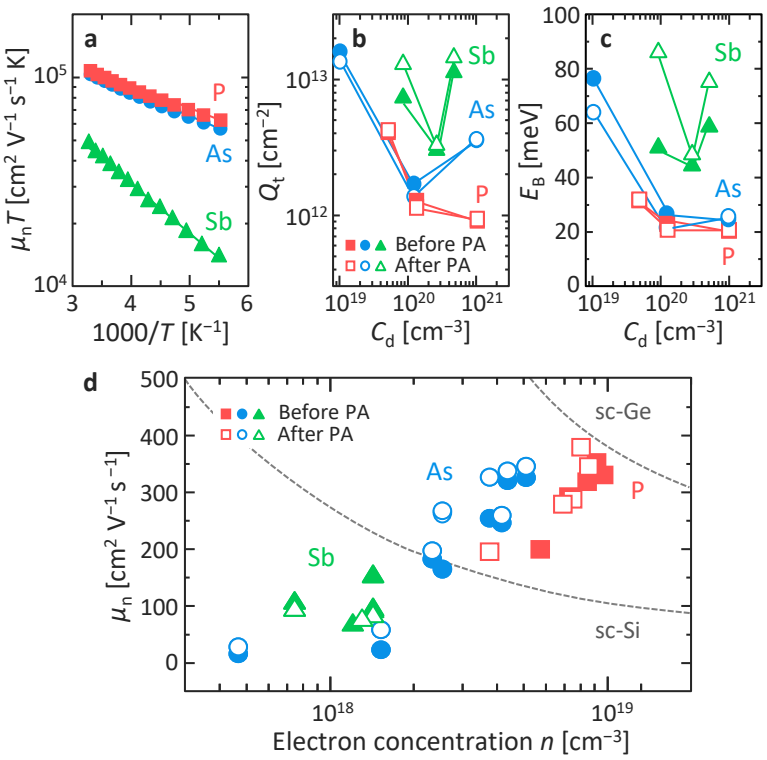

Figure 6. Electrical properties of the P-, As-, and Sb-doped Ge layers with T_d = 50 °C (As) and 125 °C (P and Sb) and T_g = 450 °C for 5 h. (a) Arrhenius plots of $\mu_n T$ of the samples with C_d = 2.0×10^{20} cm^{-3} for P, 1.2×10^{20} cm^{-3} for As, and 1.6×10^{20} cm^{-3} for Sb. (b) trap-state density Q_t and (c) energy barrier height E_B of the Ge grain boundary before and after PA (500 °C) as a function of C_d. (d) Comparison of the electron mobility μ_n and electron concentration n of the P-, As-, and Sb-doped samples obtained in this study. The dotted lines show the data for bulk single-crystal (sc-) Si and Ge wafers, which were derived from the electrical conductivity and carrier concentration in Ref. 1.

Table of Contents